Origin of banded patterns in natural sphalerite

Ivan L'Heureux
Ottawa-Carleton Institute for Physics, University of Ottawa, Ottawa, Ontario, Canada K1N 6N5
(Received 11 February 2000)

Mississippi Valley type (MVT) sphalerite is a zinc ore mineral (zinc sulfide) found in many sedimentary basins around the world. Its texture is described as a polycrystalline aggregate which results from the precipitation of metal-rich brines in a carbonate host rock. Typically, it exhibits a spatial pattern characterized by an alternation of colored bands with a length scale on the order of 0.1 mm. In our samples, the color of the bands correlates with the local iron composition. In order to understand the origin of banded patterns in MVT sphalerite, we propose here an extension of the competitive growth mechanism often used to model periodic precipitation patterns. In our model, precipitation from interacting brines, growth and dissolution of crystallite radius, and ripening are taken into account. As in all postnucleation models, the nucleation process is neglected. It is shown that our model may indeed generate patterns that are qualitatively compatible with the observed ones. This constitutes an example of self-organization in a geochemical system.

PACS number(s): 81.10.Aj, 05.45.−a, 91.65.Rg, 47.54.+r

I. INTRODUCTION

It has been known for a long time that all naturally grown minerals do not have a uniform chemical composition. Many of them exhibit complex growth patterns, such as oscillatory zoning. In oscillatory-zoned single crystals, the chemical composition varies more or less regularly from the core of the mineral to its rim. The length scales over which the pattern occurs range from tens of nanometers to several tens of micrometers. Perhaps the best known example of such compositional pattern is plagioclase feldspar, a mineral commonly found in igneous rocks [1]. In fact, oscillatory zoning has been observed in all classes of minerals [2] and in various environments such as magmatic melts and aqueous solutions.

Another type of oscillatory growth pattern results in the formation of bands of different colors, such as those observed in agates. Such a color banding is commonly found in sphalerite (ZnS) of the so-called Mississippi Valley type (MVT) variety (Fig. 1). This mineral is found in sedimentary basins all over the world and constitutes an economically important source of zinc. It is typified by the deposits of the Tri-State area (Tennessee, Missouri, Arkansas) of the United States. MVT sphalerite precipitates from low-temperature (50–100 °C) hydrothermal fluids within a carbonate host rock. The precipitation occurs in breccia (coarse-grained rock with angular fragments), solution channels, or other voids at shallow depths.

Because of the geological implications, it is important to obtain as much information as possible on the formation conditions of these oscillatory-zoned systems. Concurrently with experimental synthesis (see, e.g., [3]), modeling of the growth processes allows an understanding of these conditions. Realistic models of oscillatory zoning must take into consideration the various nonlinear feedbacks that couple the dynamical variables (see, e.g., [4]). The patterns may result from deterministic [2] or stochastic [5] changes in the external parameters, or from self-organizing internal processes (see, e.g., [6,7]), and more generally from a combination of both. The goal of this paper is to propose a phenomenological model for the formation of bands in MVT sphalerite.

Bands in MVT sphalerite are characterized by a series of alternating zones of white, yellow, brown, orange, or black layers with length scales on the order of 0.1–1 mm. In contrast to oscillatory zoning in a single mineral, the bands results from the aggregation of many crystallites. The long axes of these crystallites are oriented in a direction normal to the banding [8,9]. Previous work [9] has found that the color of the bands correlates with the iron content: the higher the ratio of Fe to (Zn+Fe), the darker the band. Analyses of samples [9] originating from Pine Point, Northwest Territories (Canada), determined that the iron and zinc contents vary, respectively, from 1.9 and 64.2 wt % for light bands, to 6.0 and 61.2 wt % for dark bands. These numbers correspond to a molar fraction of FeS to (FeS+ZnS) varying from 3% for light bands to 10% for dark bands.

Two categories of descriptive models have been proposed to explain the general conditions in which MVT deposition occurs. In the first class (''non mixing'' models) [10,11], a low-pH brine transports the metals and reduced sulfur to the deposition site. Precipitation may then be caused by sudden changes in the environment (changes in pH, temperature, or dilution). In the second class of model (''mixing''), a metal-bearing brine is transported to the deposition site and reacts with a H_2S-rich brine [11–13], resulting in a precipitation event that is possibly far from equilibrium. In general, a consideration of geological arguments and chemical reaction path modeling seem to favor the second class of model [13]. The pattern-formation model described in this paper is defined in the framework of mixing models.

We will base our model of banding pattern dynamics in sphalerite on the concept of Liesegang ring formation. In a typical Liesegang experiment [14], a salt solution A reacts in an aqueous gel with another salt B and forms a product C_{aq}. Under certain conditions, this product precipitates and forms a series of rings or bands C_s:

FIG. 1. Microphotograph in transmitted light of a thin section of MVT, sphalerite showing banding, characterized by an alternation of dark and light zones. The concentric bands form crystallite aggregates that emanate from centers of growth. The black filaments are branching galena (PbS) crystals, a mineral often associated with sphalerite. The sample originates from the Polaris mine, Northwest Territories (Canada). The vertical bar in the upper right corner corresponds to 1 mm.

$$A+B\rightarrow C_{\mathrm{aq}}\leftrightarrow C_s\,.$$

This type of pattern formation is relevant to many geological systems [4,15].

Two classes of models are usually invoked to model the formation of Liesegang bands. In prenucleation models [16], the feedback mechanism between nucleation kinetics of precipitate particles and diffusional transport of the product in solution generates a regular banding pattern, which typically obeys simple scaling laws [17]. In postnucleation models, such as the competitive growth model (CGM) [18], one assumes that the precipitate nucleation phase is terminated and that the density of nuclei is constant. A feedback between precipitate growth, diffusion of the product in solution, and surface tension effects (ripening) then produces complex banding patterns. Consider, for example, a single-component Liesegang experiment in an initially homogeneous system. Assume the existence of a small localized increase in crystallite radius. From the Gibbs-Thomson relation, this generates a local decrease in the equilibrium concentration in the solution. A net mass transport toward the perturbation is induced by diffusion, which increases the crystallite size further. But as the crystallite radius increases, the crystallites adjacent to the initial perturbation will dissolve through ripening, thus resulting in an increase of the equilibrium concentration in the zone close to the perturbation. This in turn causes a net mass flux away from that zone, which induces growth of the crystallite further away. The cycle can then be repeated further along the system. This mechanism has therefore the potential to generate banding patterns.

In this paper, we generalize the model of Liesegang ring formation to the coprecipitation of a binary solid solution constituted by two compounds (FeS and ZnS). For simplicity, we describe the precipitation dynamics in the framework of postnucleation models. A version of the CGM that can be applied to two-precipitate systems has already been proposed in Ref. [19]. In that version, however, the two precipitates form separate crystallites, each of well-defined composition. Our model allows for mixing of the two species in the precipitate. It is not the goal of this study to systematically investigate the effects of varying the parameters, but rather to show that realistic banding patterns may be generated by a simple mixing model.

The paper is organized as follows. In Sec. II, the basic equations defining the growth model are introduced. In order to relate the composition of iron in the crystallite to the concentrations in the solution, we introduce a phenomenological partitioning coefficient in the standard way. A dimensionless formulation is then presented. In Sec. III, we present a linear stability analysis on the autonomous version of the model. It is seen that, in some conditions, the system is intrinsically unstable to inhomogeneous perturbations and that no characteristic length scale can be defined at the linear level of description. In Sec. IV, we briefly describe the numerical method and present the results for two situations: one in which the crystallites radius is initially constant (except for a local perturbation) and one in which it is random. Concluding statements are presented in Sec. V. Two appendices complete the presentation.

II. MODEL

We reduce the model to one spatial dimension chosen along a direction normal to a typical band. This is expected to be a valid approximation in the common cases where the radii of curvature of the bands are large compared to the band thickness.

In the context of mixing models, we assume that an influx of (Fe-Zn)-rich brine flows into a reservoir (the porous host rock) and reacts locally with a H_2S-rich brine to produce iron-bearing sphalerite in the form of a crystallite aggregate. We choose the origin of the spatial coordinate x at the initial reaction front where both brines are mixed. The reservoir is defined for $x>0$. For example, referring to Fig. 1, the brine could be injected from a direction out of the plane of the figure in the clear area near the center of the banded aggregate. In this case, the x axis could correspond to a radial direction normal to the bands in the plane of the figure. The simplest reaction scheme is

$$\mathrm{Fe}^{2+}+\mathrm{H_2S}\xrightarrow{k_1}\mathrm{FeS_{aq}}+2\mathrm{H}^+,$$

$$\mathrm{ZnCl_2}+\mathrm{H_2S}\xrightarrow{k_2}\mathrm{ZnS_{aq}}+2\mathrm{H}+2\mathrm{Cl}^-,$$

$$m\mathrm{ZnS_{aq}}+n\mathrm{FeS_{aq}}\leftrightarrow(\mathrm{Zn}_m\mathrm{Fe}_n,\mathrm{S}_{m+n}), \tag{1}$$

where k_1 and k_2 are forward rate constants and the third reaction describes the coprecipitation of metal sulfide species as crystallites. Following Ref. [20], we assume that the Zn is transported in the first brine as a chloride complex. At the low temperatures considered, a similar complexing of iron is unlikely [20].

A. Basic equations

We choose the origin of the spatial coordinate x at the initial reaction front where both brines are mixed. The reservoir is defined for $x>0$. Let $Z(x,t)$ and $F(x,t)$ be the $ZnCl_2$ and Fe^{2+} concentration in the solution (moles per fluid volume), respectively. We introduce the porosity ϕ of the medium, which is defined as the fraction of the rock volume occupied by fluid-filled pores. We assume that the changes in the medium porosity due to the precipitation or dissolution of sphalerite are negligible. We also define V as the velocity of the advecting fluid (assumed constant), and $D_{Z,F}$ as the diffusion coefficients of $ZnCl_2$ and Fe, respectively. With t denoting time, the rate equations for F and Z are

$$\phi\frac{\partial F}{\partial t}=\phi D_F\frac{\partial^2 F}{\partial x^2}-\phi V\frac{\partial F}{\partial x}-k_1\phi F,$$

$$\phi\frac{\partial Z}{\partial t}=\phi D_Z\frac{\partial^2 Z}{\partial x^2}-\phi V\frac{\partial Z}{\partial x}-k_1\phi Z. \tag{2}$$

This set of equations is linear and can be explicitly solved with appropriate boundary and initial conditions. We use

$$F(0,t)=F_0,\quad Z(0,t)=Z_0,$$

$$F(\infty,t)=Z(\infty,t)=0,$$

$$F(x,0)=Z(x,0)=0,\quad x\neq 0. \tag{3}$$

Here, F_0 and Z_0 are the corresponding concentrations in the input brine. The solution of Eq. (2) then reads

$$\frac{F}{F_0}=\exp\left(\frac{xV}{2D_F}(1-\lambda)\right)+\frac{1}{2}\exp\left(\frac{xV}{2D_F}\right)\left[\exp\left(\frac{xV\lambda}{2D_F}\right)\times\mathrm{erfc}\left(\frac{V\lambda\sqrt{t/D_F}}{2}+\frac{x}{2\sqrt{D_F t}}\right)-\exp\left(-\frac{xV\lambda}{2D_F}\right)\times\mathrm{erfc}\left(\frac{V\lambda\sqrt{t/D_F}}{2}-\frac{x}{2\sqrt{D_F t}}\right)\right], \tag{4}$$

where

$$\lambda\equiv\left(1+\frac{4k_1D_F}{V^2}\right)^{1/2}. \tag{5}$$

A similar expression for $Z(x,t)$ is obtained by substituting Z_0 for F_0, k_2 for k_1, and D_Z for D_F.

We now model the precipitation dynamics. In the spirit of the CGM, we assume that the crystallites are approximately spherical with an effective radius $r(x,t)$ and locally monodisperse, so that r is a function of the crystallite position x and of time t. Let $B(x,t)$ and $C(x,t)$ denote the concentration (moles per fluid volume) of FeS and ZnS in solution, respectively, $D_{1,2}$ the respective diffusion coefficients, and $U_{1,2}$ the respective precipitation rates (moles precipitated per unit time per unit rock volume). Then

$$\phi\frac{\partial B}{\partial t}=\phi D_1\frac{\partial^2 B}{\partial x^2}-\phi V\frac{\partial B}{\partial x}+k_1\phi F-U_1,$$

$$\phi\frac{\partial C}{\partial t}=\phi D_2\frac{\partial^2 C}{\partial x^2}-\phi V\frac{\partial C}{\partial x}+k_2\phi Z-U_2. \tag{6}$$

In the postnucleation regime, the precipitation rates are given by

$$U_1=\frac{\partial}{\partial t}\left(\frac{4\pi}{3}\rho N r^3 p\right),$$

$$U_2=\frac{\partial}{\partial t}\left(\frac{4\pi}{3}\rho N r^3(1-p)\right). \tag{7}$$

Here, ρ is the average solid molar density, N (assumed constant) is the nuclei density (i.e., the number of precipitated nuclei per unit rock volume), and $p(x,t)$ is the composition (mole fraction) of FeS in the sphalerite crystallite aggregate.

It is this composition p that correlates with the observed band color and is the main variable of interest. It is possible to relate p to the other dynamical variables by assuming that the mole number of each component precipitated in the aggregate is proportional to its accretion velocity [4,7,21]. However, since this relation breaks down close to equilibrium when the growth velocities may vanish, we propose instead a simple relation between p and the concentration of the components in solution. We introduce the partitioning coefficients K_1 and K_2 by the standard definition:

$$n_1^s(x,t)=K_1B(x,t),\quad n_2^s(x,t)=K_2C(x,t), \tag{8}$$

where n_i^s is the concentration of FeS ($i=1$) and ZnS ($i=2$) in the solid aggregate at position x and time t. As long as a precipitate is formed (i.e., $r>0$), the composition p is

$$p=n_1^s/(n_1^s+n_2^s)=KB/(KB+C), \tag{9}$$

where $K=K_1/K_2$ is treated as a phenomenological coefficient. Physically, Eq. (9) indicates that the local composition of FeS in the crystallite is proportional to the probability of finding FeS in solution at that position.

Assuming interface-controlled kinetics, the accretion velocity of FeS into the solid aggregate, V_1, may be written for a dilute solution as (see Appendix A)

$$V_1=\beta_1[B-C_1^0(r)]. \tag{10}$$

Here β_1 is a microscopic kinetic coefficient and $C_1^0(r)$ is the concentration of FeS in solution at equilibrium with a crys-

tallite of radius r [22]. A similar expression can be written for the accretion velocity V_2 of ZnS by introducing the kinetic coefficient β_2 and the equilibrium concentration of ZnS, $C_2^0(r)$:

$$V_2=\beta_2[C-C_2^0(r)]. \tag{11}$$

The overall growth of the crystallite can be expressed as the sum of the accretion velocities (see Appendix A):

$$\frac{\partial r}{\partial t}=V_1+V_2. \tag{12}$$

Finally, the crystallite radius dependence of the equilibrium concentrations is found from the Gibbs-Thomson relation:

$$C_i^0=C_i^\infty \exp\left(\frac{2\sigma(r)\upsilon_i}{k_BTr}\right), \quad i=1,2, \tag{13}$$

where C_i^∞ is the equilibrium concentration of FeS ($i=1$) or ZnS ($i=2$) in the solution in contact with a flat crystallite, υ_i is the molecular volume of FeS ($i=1$) or ZnS ($i=2$) in the precipitate, T is temperature, k_B is Boltzmann's constant, and $\sigma(r)$ is the effective surface tension between the crystallite and the solution. Note that to a good approximation $\upsilon_1\cong\upsilon_2\cong\upsilon_2$. In principle, the effective surface tension depends on the composition p of the crystal. Application of Butler's equation [23] to a binary system leads to the following approximate expression:

$$\exp(\sigma a/k_BT)=p\exp(\sigma_1 a/k_BT)+(1-p)\exp(\sigma_2 a/k_BT), \tag{14}$$

where a is the area of the molecular unit building up the crystallite and $\sigma_{1,2}$ is the surface tension of pure FeS ($i=1$) or ZnS ($i=2$) crystals. Since p is typically small (of the order of a few percent), we will simplify Eq. (14) by taking the surface tension of pure ZnS:

$$\sigma\cong\sigma_2. \tag{15}$$

The surface tension is almost a constant that is independent of the crystallite radius r, except for small values of r, where this dependence must be considered in order to avoid an unphysical divergence of the argument of the exponential in Eq. (13). From thermodynamic arguments, Koenig [24] has derived such an expression:

$$\sigma(r)/\sigma^\infty\equiv\psi(r)=\exp\left(-\int_0^{\delta/r}2\frac{1+z+z^2/3}{1+2z(1+z+z^2/3)}dz\right), \tag{16}$$

where σ^∞ is the surface tension of a flat crystal and δ is a small microscopic size characterizing the Gibbs surface. Further simplification of the integral can be performed by Padé approximants and one finds to a good approximation (with a maximum relative error of 0.8%) [25]

$$\psi(r)\cong\frac{r^2+\delta r}{r^2+3\delta r+\delta^2/\alpha}, \tag{17}$$

where $\alpha=0.3043$. As expected, $\sigma(r\to\infty)/\sigma^\infty=1$ and $\sigma(r\to0)/\sigma^\infty=\alpha r/\delta$. The latter relation ensures that the argument of the exponential in Eq. (13) is finite for small r. Equation (17) will be used in the numerical computations.

Reasonable boundary conditions for the concentration fields are the following. We assume that there is no matter flux of ZnS_{aq} and FeS_{aq} at the origin of the reacting reservoir, where the input brines are injected in the reservoir. We also assume that, far from the origin of the reservoir, there are no concentration gradients, so that only the advective term contributes to the matter flux at $x\to\infty$.

In summary, the dynamics of the system are described in terms of three variables B, C, and r. Their evolution equation is given by Eq. (6) subject to the forcing reaction terms Eq. (4) and its analog for Z, together with Eqs. (7), and (10)–(12). Once B and C are known, the local FeS composition in the solid phase p is computed through Eq. (9).

B. Dimensionless formulation

In the sum of both Eqs. (6), the term involving p disappears. It is thus convenient to introduce the sum of the concentrations in solution, E:

$$E=B+C. \tag{18}$$

We scale the time variable by a time scale τ, the crystallite radius by a radius scale $\overline{R}$, all concentration variables by the concentration scale C_1^∞, and the position variable by $L=\sqrt{D_Z\tau}$. We introduce the dimensionless parameters

$$v=V\tau/L,\quad \kappa_i=k_i\tau,\quad d_i=D_i/D_z,$$

$$b=\beta_2/\beta_1,\quad G=\frac{4\pi\overline{R}^3N\rho}{3\phi C_1^\infty}, \tag{19}$$

and the capillary lengths nondimensionalized by the radius scale

$$\gamma_i=\frac{2\sigma^\infty\upsilon_i}{k_BT\overline{R}},\quad i=1,2. \tag{20}$$

For large crystallite curvature, the argument in the exponential of the equilibrium concentrations may be expanded, so that the radius dynamics occur over a small time scale, proportional to γ_1, say. It is then convenient to further scale the concentrations by a factor γ_1:

$$\hat{B}=B/\gamma_1,\quad \hat{C}=C/\gamma_1,\quad \hat{E}=\hat{B}+\hat{C}. \tag{21}$$

Finally, we choose the time scale so as to simplify the radius evolution equation,

$$\tau=\frac{\overline{R}}{C_1^\infty\beta_1\gamma_1}, \tag{22}$$

and the radius scale so as to simplify the concentration equation,

$$\overline{R}=\left(\frac{3\phi C_1^\infty\sigma^\infty\upsilon_1}{2\pi N\rho k_BT}\right)^{1/4}. \tag{23}$$

Eliminating $\hat{C}$ in favor of $\hat{E}$, the resulting scaled evolution equations are then given by

$$\frac{\partial \hat{B}}{\partial t} = d_1 \frac{\partial^2 \hat{B}}{\partial x^2} - 3pr^2 \frac{\partial r}{\partial t} - r^3 \frac{\partial p}{\partial t} - v \frac{\partial \hat{B}}{\partial x} + \frac{\kappa_1}{\gamma_1} \frac{F}{C_1^\infty}, \tag{24a}$$

$$\frac{\partial \hat{E}}{\partial t} = d_2 \frac{\partial^2 \hat{E}}{\partial x^2} + (d_1 - d_2) \frac{\partial^2 \hat{B}}{\partial x^2} - 3r^2 \frac{\partial r}{\partial t} - v \frac{\partial \hat{E}}{\partial x} + \frac{\kappa_1}{\gamma_1} \frac{F}{C_1^\infty} + \frac{\kappa_2}{\gamma_1} \frac{Z}{C_1^\infty}, \tag{24b}$$

$$\frac{\partial r}{\partial t} = (1-b)[\hat{B} - \hat{B}_0(r)] + b[\hat{E} - \hat{E}_0(r)], \tag{24c}$$

where the scaled equilibrium concentrations are

$$\hat{B}_0(r) = \frac{1}{\gamma_1} \exp[\gamma_1 \psi(r)/r],$$

$$\hat{E}_0(r) = \hat{B}_0(r) + \frac{\Delta}{\gamma_1} \exp[\gamma_2 \psi(r)/r], \tag{25}$$

with $\psi(r)$ defined in Eq. (16) and

$$\Delta = C_2^\infty / C_1^\infty . \tag{26}$$

The FeS composition in the crystallite is again

$$p = \frac{K\hat{B}}{(K-1)\hat{B} + \hat{E}} \quad \text{if} \quad r > 0. \tag{27}$$

Finally, the boundary conditions take the form

$$d_1 \left. \frac{\partial \hat{B}}{\partial x} \right|_{x=0} - v\hat{B}(0,t) = 0,$$

$$d_2 \left. \frac{\partial \hat{C}}{\partial x} \right|_{x=0} - v\hat{C}(0,t) = 0,$$

$$\left. \frac{\partial \hat{B}}{\partial x} \right|_{x=\infty} = \left. \frac{\partial \hat{C}}{\partial x} \right|_{x=\infty} = \left. \frac{\partial \hat{E}}{\partial x} \right|_{x=\infty} = 0. \tag{28}$$

The second boundary condition written in terms of $\hat{E}$ becomes

$$d_2 \left(\left. \frac{\partial \hat{E}}{\partial x} \right|_{x=0} - \left. \frac{\partial \hat{B}}{\partial x} \right|_{x=0} \right) + v[\hat{B}(0,t) - \hat{E}(0,t)] = 0. \tag{29}$$

Typical values of the parameters are given in Table I. The order of magnitude of the growth rate scale $\beta_1 C_1^\infty$ is estimated from typical Liesegang growth rate experiments [26]. The flow velocity is estimated from Ref. [27], the rate constants from Ref. [20], and the nucleus density for typical geological systems from Ref. [15]. Typical fluid metal concentrations are taken from Refs. [13], [20]. The equilibrium concentration C_2^∞ for ZnS_{aq} is found from the solubility data of Ref. [20], assuming a pH of 5, a H_2S activity equal to $0.01M$, and a Cl^- activity of $1.0M$. These values are typical of hydrothermal ore-forming solutions [13,20]. Finally, the equilibrium concentration C_1^∞ for FeS_{aq} is estimated from the fact that approximately 1000 times more zinc sulfide than iron sulfides precipitates in the chemical reaction path modeling of Ref. [13]. A solution density of 1 kg/l has been used to convert ppm units to mole/cm^3. With these values, one finds that the radius scale $\bar{R} \approx 10^{-5}$ cm (or 33 times the scaled capillary length), the time scale $\tau \approx 3 \times 10^4$ s, and the length scale $L \approx 0.1$ cm, which is of the order of the band spacing.

TABLE I. Estimate of the parameters used in this study.

$\beta_1 C_1^\infty$	10^{-8} cm/s	σ	200 erg/cm^2
T	100 °C	N	10^5 cm^{-3}
ϕ	0.5	v	3.98×10^{-23} cm^3
D_Z	10^{-6} cm^2/s	F_0	10^{-9} mole/cm^3
D_F	2.6×10^{-6} cm^2/s	Z_0	10^{-8}–10^{-7} mole/cm^3
D_1, D_2	0.8×10^{-6} cm^2/s	ρ	0.042 mole/cm^3
V	3×10^{-6} cm/s	C_1^∞	10^{-9} mole/cm^3
k_1, k_2	10^{-2}–10^3 s^{-1}	C_2^∞	10^{-12} mole/cm^3

III. LINEAR STABILITY ANALYSIS

In order to investigate further the properties of the dynamical system, it is useful to perform a linear stability analysis on its autonomous version, i.e., a preexisting precipitate without the reaction-forcing terms $F(x,t)$ and $Z(x,t)$.

We first study the spatially homogeneous solutions of the system Eq. (24). It is easily seen that Eqs. (24a) and (24b) lead to two conservation laws

$$\hat{E} + r^3 = s_0, \quad \hat{B} + pr^3 = s_1, \tag{30}$$

where s_0 and s_1 are positive constants ($s_0 > s_1$). Setting the right-hand side of Eq. (24c) equal to 0 allows the determination of the steady state solution $(\hat{B}_s, \hat{E}_s, r_s)$:

$$(1-b)[\hat{B}_s - \hat{B}_0(r_s)] + b[\hat{E}_s - \hat{E}_0(r_s)] = 0. \tag{31}$$

Thus, by eliminating $\hat{B}_s$ and $\hat{E}_s$ with the help of Eqs. (30) and (25) in Eq. (31), one obtains a nonlinear function of r_s whose roots (with $r_s \leqslant s_0^{1/3}$) give the steady state solutions of the system. For instance, with $b = 1$, taking $\gamma_1 = \gamma_2$ and expanding the exponentials, this nonlinear function of r_s is simply

$$r_s^3 + (1+\Delta) \frac{\psi(r_s)}{r_s} - s_0 + (1+\Delta)/\gamma_1 = 0. \tag{32}$$

This function exhibits a minimum at $r_{\min}$. One therefore has zero, one, or two steady states depending on the value of $s_0 - (1+\Delta)/\gamma_1$ (Fig. 2).

More generally, for $b \neq 1$ (but still with $\gamma_1 = \gamma_2$), the steady states are given by the intersections of the two following equivalent $\hat{B}_s$ functions:

$$\hat{B}_s=\frac{1}{2(K-1)}(s_1(K-1)-s_0-r_s^3(K-1)\pm\{[s_1(K-1)-s_0-r_s^3(K-1)]^2+4(K-1)s_1(s_0-r_s^3)\}^{1/2}),$$

$$\hat{B}_s=\frac{(1+b\Delta)}{\gamma_1(1-b)}\exp[\gamma_1\psi(r_s)/r_s]-\frac{b}{1-b}(s_0-r_s^3). \quad (33)$$

The first equation is obtained by eliminating $\hat{E}_s$ and p from Eqs. (30) and (27) and solving for the resulting quadratic equation, whereas the second relation is obtained from Eqs. (31) and (25). Using this graphical method, we find that the number of steady state solutions can vary from 0 to 4, depending on the values of the parameters and of the constants s_0 and s_1.

If these steady state homogeneous solutions exist, their stability to spatiotemporal perturbations can be inferred by linearizing the equations of motion about the steady state $(\hat{B}_s,\hat{E}_s,r_s)$. We thus assume

$$\hat{B}(x,t)=\hat{B}_s+\delta_B\exp(\omega t+ikx), \quad (34)$$

where δ_B is a small perturbation amplitude, k its wave vector, and ω its time eigenvalue. δ_E and δ_r are similarly introduced for the perturbation amplitudes corresponding to the variables $\hat{E}$ and r. Expanding the exponentials in the radius growth law, the linearized system takes the form

$$\begin{pmatrix} \omega+d_1k^2+ikv+KT_s\hat{E}_sr_s^3\omega & -KT_s\hat{B}_sr_s^3\omega & 3p_sr_s^2\omega \\ k^2(d_1-d_2) & \omega+d_2k^2+ikv & 3r_s^2\omega \\ b-1 & -b & \omega-\psi_s\dfrac{(1+b\Delta)}{r_s^2}+\dfrac{(1+b\Delta)}{r_s}\psi' \end{pmatrix}\begin{pmatrix}\delta_B\\ \delta_E\\ \delta_r\end{pmatrix}=0. \quad (35)$$

Here, $T_s\equiv[(K-1)\hat{B}_s+\hat{E}_s]^{-2}$, $\psi'=d\psi/dr_s$, $\psi_s=\psi(r_s)$, and $p_s=p(\hat{B}_s,\hat{E}_s)$ is the composition at the steady state. The eigenvalues are the solutions of a cubic equation of the form

$$0=\omega^3+\omega^2(Q_1+Q_2k^2+iQ_3k)+\omega(Q_4k^2+Q_5k^4+iQ_6k+iQ_7k^3)+Q_8k^2+Q_9k^4+iQ_{10}k^3, \quad (36)$$

where the quantities Q_i are given in Appendix B and do not depend on k. It is obvious that the eigenvalues corresponding to homogeneous perturbations ($k=0$) are $\omega_1=\omega_2=0$ and $\omega_3=-Q_1$. The doubly degenerate zero eigenvalue corresponds to the two conservation laws of Eq. (30). We also see that, if $Q_1<0(>0)$, the steady state solution is unstable (stable) with respect to homogeneous perturbations. For instance, in the example of Fig. 2 with $b=1$, one finds that the steady states, defined on the branch for which the r_s is larger than $r_{\min}$, are stable with respect to homogeneous perturbations, whereas the ones defined on the other branch are unstable.

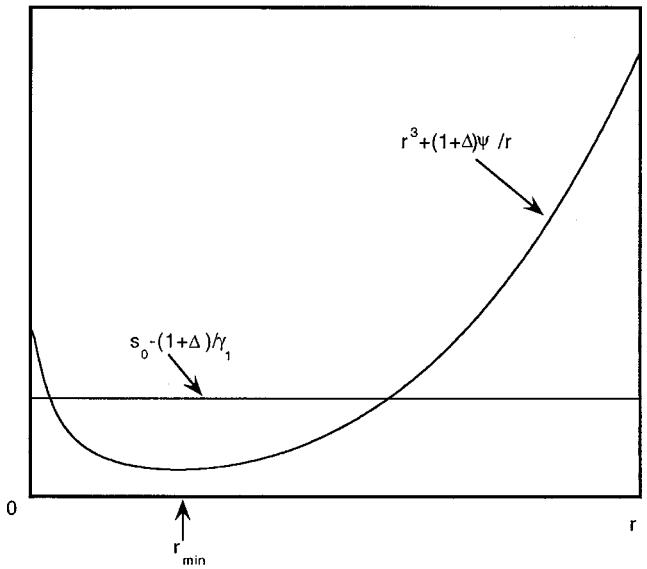

FIG. 2. Graph illustrating the method for finding the homogeneous steady states of the system (24) without reaction-forcing terms $[F(x,t)=Z(x,t)=0]$ for the special case $b=1$. Here, two steady states are found at the intersections of the curve $r^3+(1+\Delta)\psi/r$ and the horizontal line $s_0-(1+\Delta)/\gamma_1$.

The stability of the steady state to general inhomogeneous perturbations can also be studied. It turns out that in all investigated cases, the dispersion relation Re (ω), as a function of the wave vector, has one of the forms shown in Fig. 3. It is easy to show that two eigenvalue branches are stable for large k but the other branch saturates at a finite positive value ω_∞. Indeed, for large k, an asymptotic constant solution of Eq. (36) is

$$\omega_\infty\cong-\frac{Q_9}{Q_5}=\frac{(1+b\Delta)}{r_s^2}(\psi_s-r_s\psi'). \quad (37)$$

By using the exact expression Eq. (16) for ψ_s, it is then seen that ω_∞ is positive. For the cases where the steady state is unstable at $k=0$, it is easy to show that $\omega_\infty>-Q_1$ so that the dispersion curve has its maximum at large k.

The form of the dispersion relation is similar to the one found in other periodic precipitation problems based on CGM [17]. We can then conclude that (i) the system is intrinsically unstable to small perturbations and (ii) no length scale is selected, at least at this linear level of description. Thus, the system has the potential to generate complex spatio-temporal patterns.

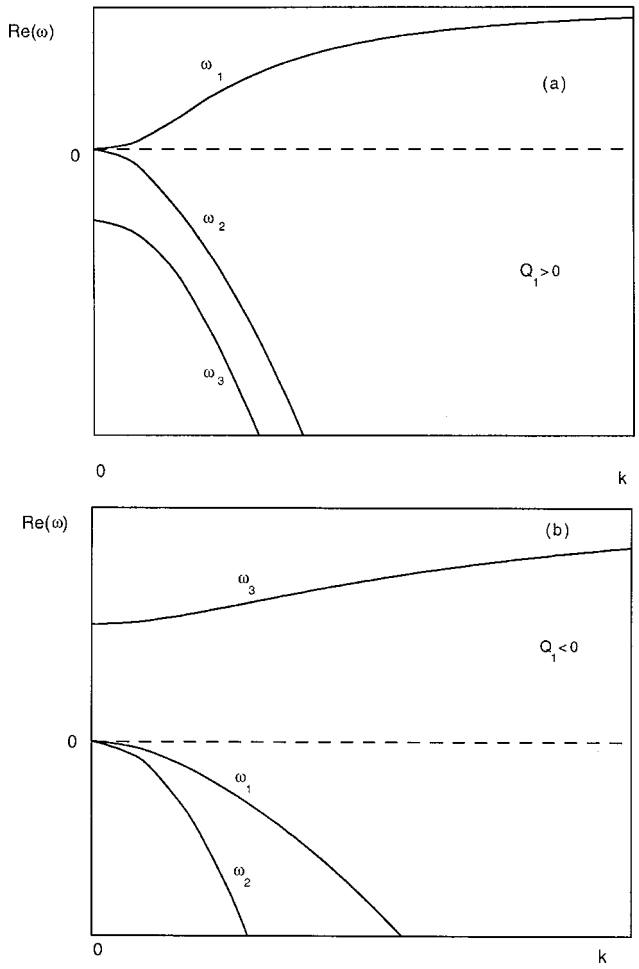

FIG. 3. Dispersion curves Re(ω) as a function of the wave number k computed from Eq. (36). In (a), $Q_1>0$ and the steady states are stable to homogeneous ($k=0$) perturbations. However, the branch ω_1 is unstable to inhomogeneous perturbations. In (b), $Q_1<0$ and the branch ω_3 is unstable to all perturbations.

IV. NUMERICAL RESULTS

A. Numerical method

In order to investigate the nature of the linearly unstable solutions in an unforced homogeneous system as well as in the forced system, we devised a numerical scheme for solving Eqs. (24), where $\partial p/\partial t$ was eliminated with the help of Eq. (27). We discretized the time and space variables using a fixed time step Δt and a space step Δx with a spatial grid of dimension M. We used centered differences for the spatial derivatives and a semi-implicit scheme (Crank-Nicholson), which requires the evaluation of all terms at intermediate half time steps. Let $\mathbf{X}^n$ be the $3M$-dimensional column vector constructed with the variables $(r,\hat{B},\hat{E})$ evaluated at time $n\Delta t$. To deal with the nonlinearities, we adopted a noniterative forward projection method [28]. This scheme consists in evaluating $\mathbf{X}^{n+1/2}$ at intermediate half time steps by the following approximation applied only to the nonlinear terms:

$$\mathbf{X}^{n+1/2}\cong\mathbf{X}^n+\frac{\Delta t}{2}\frac{\partial\mathbf{X}^n}{\partial t}. \tag{38}$$

We thus obtained a discretized version of Eqs. (24) and their boundary conditions, which takes the form of the following matrix equation:

$$\mathbf{A}(\mathbf{X}^n)\cdot\mathbf{X}^{n+1}=\mathbf{B}(\mathbf{X}^n). \tag{39}$$

Here, $\mathbf{B}(\mathbf{X}^n)$ is a $3M$-dimensional column vector and $\mathbf{A}(\mathbf{X}^n)$ is a $3M\times3M$ matrix. **B** and **A** depend only on previously known **X**. Moreover, **A** can always be arranged in the form

$$\mathbf{A}=\begin{pmatrix}\mathbf{T} & 0\\ \mathbf{0} & \mathbf{1}\end{pmatrix}, \tag{40}$$

where **1** is an $M\times M$ identity matrix and **T** is a $2M\times2M$ bi-tridiagonal matrix. **T** corresponds to the two diffusion equations (24a) and (24b). The numerical solution was thus obtained by straightforward successive inversions of bi-tridiagonal matrices [29] starting from known initial conditions. The scheme was stable and convergent for the range of parameters considered.

B. Coarsening in an initially homogeneous sol

In order to verify the linear stability analysis of Sec. III, we first considered the case where the forcing reaction terms were turned off ($F_0=Z_0=0$) and the initial condition was chosen to be homogeneous except for a local perturbation. Specifically, the initial concentrations were constant in space, whereas the initial radius was constant everywhere but at the origin. Physically, this initial value would result from the prenucleation phase of the precipitation, the dynamics of which is outside the scope of Eqs. (24).

Figure 4 illustrates the numerical solution obtained with

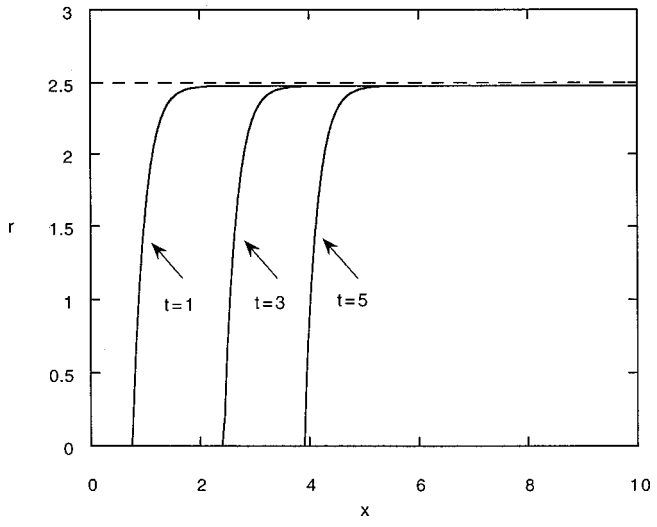

FIG. 4. Time evolution of the crystallite radius spatial dependence in the absence of reaction-forcing terms and for an initially uniform system. The initial dimensionless radius (dashed line) was $r(x,0)=2.5$ except at the origin where $r(0,0)=2.0$. The parameters were chosen as $b=1$, $K=1$, $d_1=d_2=0.8$, $v=0.9$, $\Delta=10^{-3}$, $\gamma_1=\gamma_2=0.03$, and $\delta=\gamma_1/2$. The initial dimensionless concentrations were $\hat{E}(x,0)=33.367$ and $\hat{B}(x,0)=33.333$, corresponding to dimensionalized initial concentrations $B(x,0)=C_1^\infty$ and $C(x,0)=C_2^\infty$. For computational purposes, the time step was $\Delta t=0.0001$, the space step was $\Delta x=0.05$, and $M=200$ spatial grid points were considered.

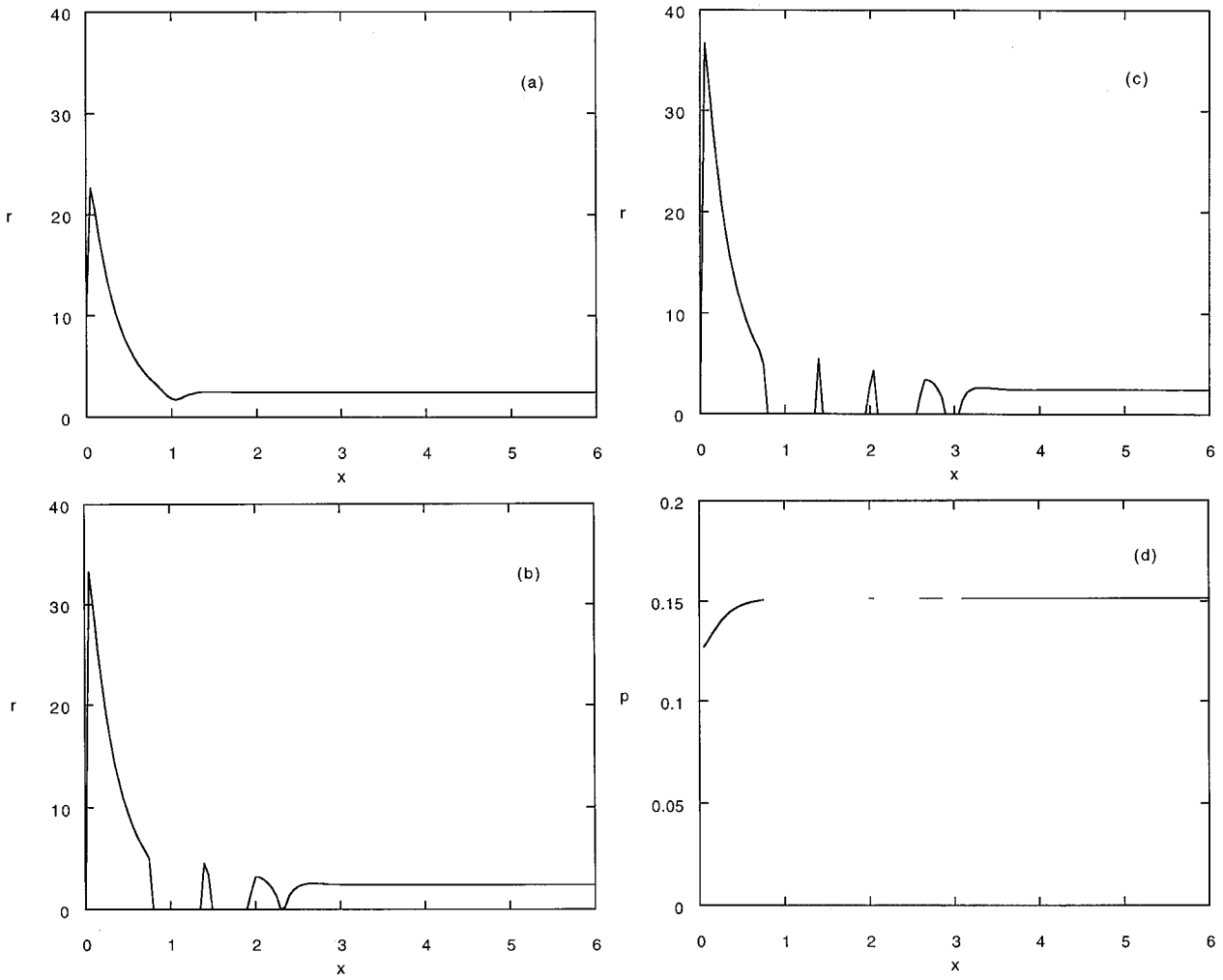

FIG. 5. Formation of bands for an initially uniform system but in presence of the reaction-forcing terms $F(x,t)$ and $Z(x,t)$. The parameter values and initial conditions are the same as in Fig. 4 with, in addition, $D_F/D_Z=2.6$, $\kappa_1=\kappa_2=100$, $F_0/\gamma_1 C_1^{\infty}=1$, and $Z_0/\gamma_1 C_1^{\infty}=10$. The time evolution of the crystallite radius is illustrated for $t=36$ (a), 108 (b), and 144 (c). (d) illustrates the FeS composition as a function of space at $t=144$. In the interband regions [where $r(x,t)=0$], the composition is not defined.

$b=1$ and in a case for which Eq. (32) gives two homogeneous steady states ($r_s=0.027$ and 2.478 in this example). In Sec. III, we saw that the steady state with the largest radius is stable to homogeneous perturbations [Fig. 3(a)], whereas the other one is unstable [Fig. 3(b)]. However, the former is unstable to inhomogeneous perturbations. In Fig. 4, the crystallite radius is plotted as a function of space for various times. The linear stability behavior is clearly illustrated by the figure: for small times, the crystallite radius stays at the value 2.478 for a significant spatial range. However, near the origin, the perturbation is unstable, and the radius decreases to zero. Eventually, the zero-radius solution dominates: the system dissolves completely.

Figures 5(a)–5(c) illustrate a typical case for which the reaction-forcing terms are present. The initial conditions are the same as in Fig. 4. Here, the situation is more interesting: as time evolves, the solution evolves toward a periodic succession of oscillations characterized by narrow peaks for which the radius is significantly different from zero. In the example shown here, the pattern wavelength is 0.65 reduced units. We saw in Sec. III that the linear stability analysis did not yield any length scale. Also, the forcing term intervenes in a linear fashion in the equations of motion. Thus, the observed pattern length scale is a strictly nonlinear manifestation that results from the competition between the forcing terms (which favor precipitation) and the dissolution. Figure 5(d) shows the FeS composition profile p at a specific time for the case discussed above. Since the radius is nonzero in the precipitate, the iron composition $p(x,t)$ also exhibits a band structure bounded by the regions where the radius is zero [Eq. (27)]. However, in the interband region, the FeS composition is essentially constant in time and uniform in space.

Figure 6 illustrates a situation identical to Fig. 5, except that the initial radius is smaller. This choice corresponds to the case where no homogeneous steady state exists. Here, a band develops in the vicinity of the initial perturbation. As time increases, the band becomes narrower and the maximum radius increases. Further away from this band, the system dissolves. No oscillating pattern is observed in this case. Thus, we have illustrated that the system can coarsen in the presence of forcing reaction terms, but its ability to exhibit banded patterns depends on the initial conditions.

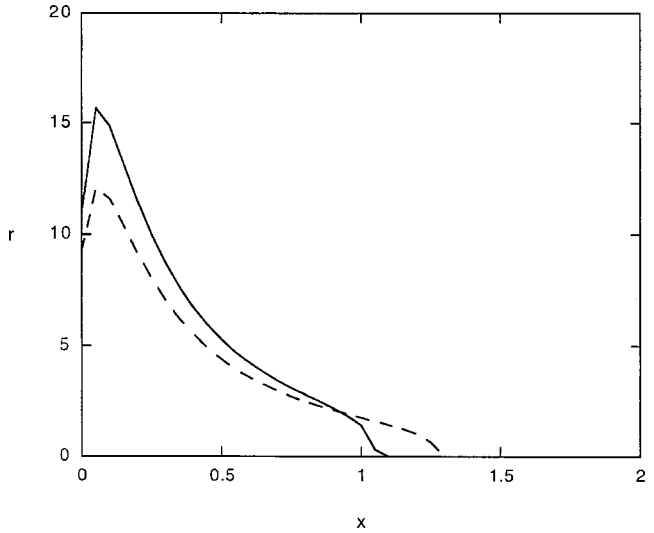

FIG. 6. Evolution of the crystallite radius for an initially uniform system in presence of reaction-forcing terms, but for a case where no homogeneous steady state exists. The parameter values and initial conditions are as in Fig. 5, except $r(x,0)=1.0$, $r(0,0)=0.9$. The dashed line gives the radius at $t=2$, whereas the continuous line corresponds to $t=4$.

C. Coarsening of sphalerite

The uniformly constant initial radius case discussed above may not be representative of the conditions in which MVT sphalerites are expected to form. As mentioned in the Introduction, the mixing model assumes that MVT sphalerite results from the precipitation of two brines interacting in a brecciated host rock. In order to mimic the disorder inherent to this type of geometry, we rather assume that the radius of the crystallites resulting from the prenucleation phase of the precipitation was random. Specifically, the initial radius was chosen as

$$r(x,0)=r_0+\xi(x), \tag{41}$$

where r_0 is its average value and ξ represent random fluctuations sampled at each grid site from a uniform distribution over the range $[r_0-A/2,r_0+A/2]$. This constitutes the initial condition for the growth and ripening processes of sphalerite described by Eqs. (24).

Figures 7(a) and 7(b) show plots of the iron composition of the sphalerite aggregate as a function of space at two different times for a typical case in the presence of reaction terms. Near the origin, the composition is almost pure ZnS. But elsewhere we note the presence of complex composition oscillations. Also, the interband regions where no precipitate is found (r being null) are much thinner than in the case of Fig. 5. Of course, these oscillations have a random character, but periodic spatial components also develop in time, as shown by the Fourier transform (power spectrum) in Fig. 7(c). In this case, the signal has many well-defined peaks, the first three (excluding the zero-wave-number peak) being at reduced wave numbers of about 1.25, 1.562, and 1.875 units. These correspond to dimensionalized wavelengths of 0.08, 0.064, and 0.053 cm. It is interesting to note that the third, fifth, and sixth peaks can be derived from harmonic combinations of the first two: $(1.562-1.25)+1.562\approx 1.875$,

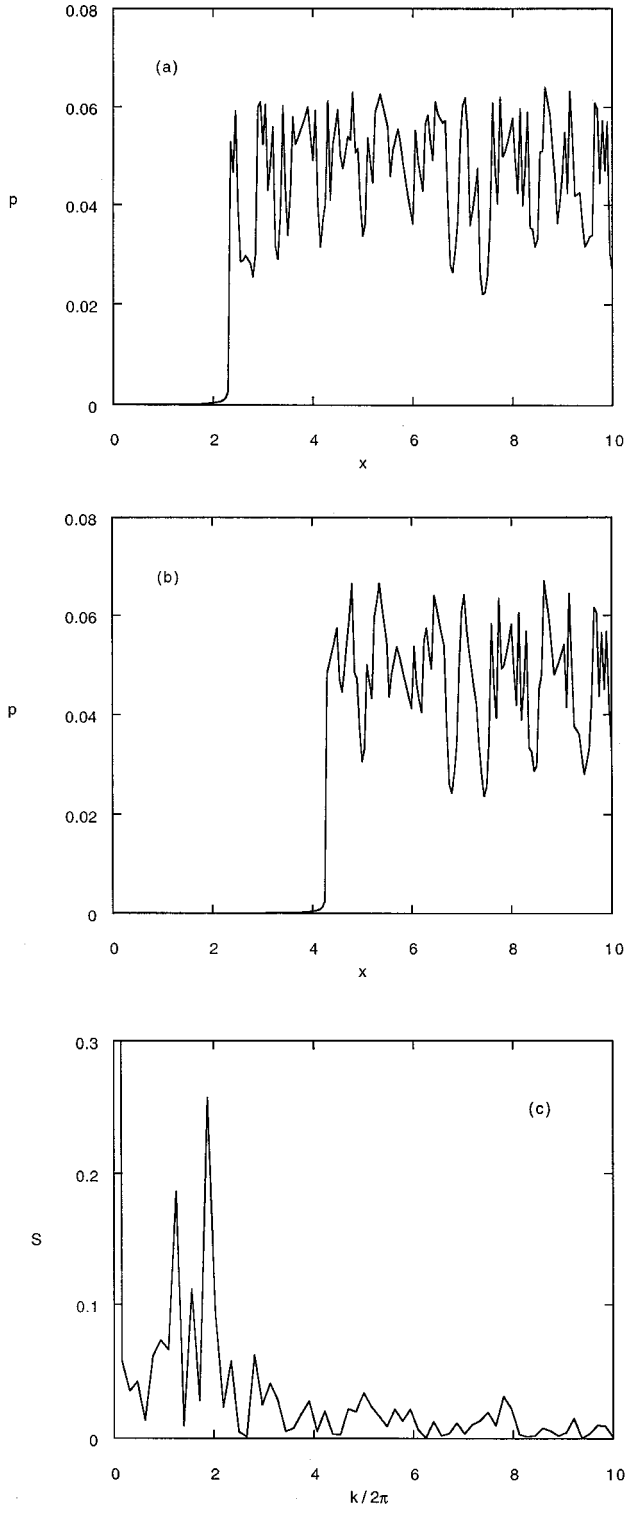

FIG. 7. Formation of compositional bands in presence of reaction-forcing terms with initially random crystallite radius [Eq. (41)], with $r_0=A=10$. The parameter values and the other initial conditions are as in Fig. 5, except that $K=6\times10^{-5}$. (a) and (b) show the FeS composition profile at dimensionless times $t=20$ and 40, respectively. (c) gives the power spectrum S of the Fourier transform of the last 128 data points of the profile of (a) in terms of the reduced wave number $k/2\pi$. The zero-wave-number peak lies outside the range of the graph. For the purpose of computing the Fourier transform, the composition profile was linearly interpolated in the thin regions where the radius vanishes.

$1.562+1.25=2.812$, and $1.875+1.25=3.125$. This supports the view that the spectrum results from nonlinear interactions between the modes. Also, the composition varies between about 3 and 6 mol% FeS. These features are qualitatively consistent with the characteristics of observed MVT bands. Finally, as time increases, the composition instability front moves outward. Eventually, the composition evolves toward pure ZnS.

Similar banding patterns are also obtained for other values of K and b, as long as b is not too large ($b<10$) and K is small enough ($K<10^{-4}$). In general, decreasing the value of K for b fixed at 1 decreases the composition fluctuations as well as its average value. For fixed K and b, banded patterns were generated for all initial radius random amplitudes A and the power spectrum peaks were at the same wave-number values as above. However, the time necessary to achieve a banded pattern was larger for a larger amplitude A. This can be explained in terms of the inverse of the saturation eigenmode $T_\infty \equiv 1/\omega_\infty$, with ω_∞ defined in Eq. (37). The quantity T_∞ gives the time scale over which a homogeneously stable steady state loses its stability to inhomogeneous perturbations. For large initial radius, the quantity s_0, defined in Eq. (30), is large. But the larger s_0, the larger the steady state radius [Eq. (32)], which yields a larger T_∞, in agreement with the numerical findings.

V. CONCLUSION

In this paper, we have proposed an application of the competitive growth theory of precipitation that models the formation of banded patterns in MVT sphalerite. Using geologically relevant values of the known parameters, the numerical simulations show the existence of spontaneous band formation in the crystallite radius spatial distribution in a chemically forced system. In order to generate banded patterns in the FeS composition, random initial conditions in the crystallite radius were necessary. The composition patterns generated have dominant wavelengths that are consistent with the order of magnitude of the band spacing observed in natural samples. The model helps clarify the circumstances in which MVT sphalerite ore is formed and is consistent with the mixing of two different brines interacting in a host rock.

In our model, only ripening, growth, and chemical reactions are considered. As is typical of postnucleation models, interband regions with no precipitate ($r=0$) often develop. However, our approach neglects nucleation processes (except implicitly in defining the initial conditions). A more realistic model should include nucleation, growth, and ripening processes in a unifying way. Such a theory has been proposed for the periodic precipitation of a single component in Ref. [25] and could be extended for the MVT case.

A basic assumption of our model is that the FeS composition is only related to the local solution concentration environment [Eq. (27)]. This assumption introduces a phenomenological parameter, the ratio of the partitioning coefficients K [Eq. (9)]. Although this is a reasonable hypothesis, a more realistic approach could relate the crystallite composition to the relative growth or dissolution velocities of the ZnS and FeS species. This is currently under investigation.

ACKNOWLEDGMENTS

This research was supported by a grant from the Natural Sciences and Engineering Research Council of Canada. The author wishes to thank Brian Logan for reading the manuscript and Anthony Fowler for fruitful discussions and for preparing Fig. 1. Maurice Chacron is thanked for assistance in the numerical computations.

APPENDIX A: ACCRETION VELOCITIES

For simplicity, we assume that the crystallite grows through a normal process (see, e.g., [22]) and that the kinetics is interface controlled (diffusion-controlled growth could be considered as well). The frequency of attachment of FeS units onto the surface of the crystallite is an activated process and can be written as

$$\omega_+ = \nu B v_1 e^{-\Delta u_1/k_B T}, \tag{A1}$$

where ν is a frequency of vibration of the surface, v_1 is the molecular volume of FeS in the solid phase, and ΔU_1 is the energy barrier associated with the transfer of one FeS unit from the solution to the crystallite. The product Bv_1 is essentially the probability of finding a FeS unit in solution in the vicinity of the attachment site. The detachment frequency is

$$\omega_- = \nu(1-Bv_1-Cv_2)e^{-(\Delta U_1+\Delta h_1)/k_B T}, \tag{A2}$$

where Δh_1 is the molecular enthalpy of transition and v_2 is the molecular volume of ZnS in the solid phase. The factor $(1-Bv_1-Cv_2)$ is the probability that the space around the detachment site is free of solute particles.

At equilibrium, both frequencies are equal and

$$e^{-\Delta h_1/k_B T} = \frac{C_1^0 v_1}{1-C_1^0 v_1 - C_2^0 v_2}, \tag{A3}$$

where C_i^0 are the concentrations of FeS ($i=1$) and ZnS ($i=2$) in equilibrium with the crystallite. Letting l_1 be the typical size of the FeS molecule and P be the probability of finding a kink site on the surface of the crystallite, the net accretion rate (m/s) of FeS is then

$$V_1 = l_1 P(\omega_+ - \omega_-) = \frac{\nu l_1 P}{C_1^0} e^{-(\Delta U_1+\Delta h_1)/k_B T} \times \left(B - C_1^0 - B\sum_{i=1}^{2} C_i^0 v_i + C_1^0(Bv_1+Cv_2) \right). \tag{A4}$$

For dilute solutions, we can neglect the last three terms in the sum in the right-hand side and finally obtain Eq. (10):

$$V_1 = \beta_1(B - C_1^0), \tag{A5}$$

where

$$\beta_1 = \frac{\nu l_1 P}{C_1^0} e^{-(\Delta U_1+\Delta h_1)/k_B T} \tag{A6}$$

is the kinetic coefficient, considered here as a phenomenological parameter. A similar expression is obtained for the accretion of ZnS [Eq. (11)].

We can easily relate the growth of the crystallite to the accretion rates. The volume of the crystallite is

$$\frac{4\pi}{3}r^3=\sum_{i=1}^{2}\upsilon_i N_i^s, \tag{A7}$$

where N_i^s is the number of molecules of FeS ($i=1$) and ZnS ($i=2$) in the crystallite. The time derivative of Eq. (A7) gives

$$4\pi r^2\frac{\partial r}{\partial t}=\sum_{i=1}^{2}\upsilon_i\frac{\partial N_i^s}{\partial t}. \tag{A8}$$

But

$$\frac{\partial N_i^s}{\partial t}=\frac{V_i 4\pi r^2}{\upsilon_i}. \tag{A9}$$

Therefore

$$\frac{\partial r}{\partial t}=\sum_{i=1}^{2}V_i \tag{A10}$$

which is Eq. (12).

APPENDIX B: COEFFICIENTS Q_i

For completeness, we write the detailed expressions for the quantities Q_i appearing in Eq. (36):

$$Q_1=\Lambda^{-1}\left(-\frac{\tilde{\psi}}{r_s^2}\Lambda+3br_s^2(1-p_s)+3p_sr_s^2+3p_sr_s^2+3T_sKr_s^5(\hat{B}_s+b\hat{C}_s)\right),$$

$$Q_2=\Lambda^{-1}[d_2+KT_sr_s^3(d_1\hat{B}_s+d_2\hat{C}_s)],$$

$$Q_3=\Lambda^{-1}\upsilon(2+K\hat{E}_sT_sr_s^3),$$

$$Q_4=\Lambda^{-1}\left(-(d_1+d_2)\frac{\tilde{\psi}}{r_s^2}-KT_s\tilde{\psi}r_s(d_1\hat{B}_s+d_2\hat{C}_s)-\upsilon^2+3bd_1(1-p_s)r_s^2+3d_2p_sr_s^2\right),$$

$$Q_5=\frac{d_1d_2}{\Lambda},$$

$$Q_6=\Lambda^{-1}\upsilon\left(-2\frac{\tilde{\psi}}{r_s^2}-K\hat{E}_sT_s\tilde{\psi}r_s+3br_s^2+3p_sr_s^2(1-b)\right),$$

$$Q_7=\frac{\upsilon}{\Lambda}(d_1+d_2),$$

$$Q_8=\frac{\tilde{\psi}\upsilon^2}{\Lambda r_s^2},$$

$$Q_9=-\frac{d_1d_2\tilde{\psi}}{\Lambda r_s^2},$$

$$Q_{10}=-(d_1+d_2)\frac{\tilde{\psi}\upsilon}{\Lambda r_s^2}, \tag{B1}$$

where $T_s=[(K-1)\hat{B}_s+\hat{E}_s]^{-2}$, $\Lambda=1+K\hat{E}_sT_sr_s^3$, $\tilde{\psi}=(\psi_s-r_s\psi')(1+b\Delta)$, and $\hat{C}_s=\hat{E}_s-\hat{B}_s$ is the steady state value of the ZnS dimensionless concentration.

[1] T. H. Pearce, Can. Mineral. **22**, 383 (1984); T. H. Pearce, J. K. Russell, and I. Wolfson, Am. Mineral. **72**, 1131 (1987); T. H. Pearce and A. H. Clark, Geology **17**, 757 (1989); T. H. Pearce and A. M. Kolisnik, Earth-Sci. Rev. **29**, 9 (1990).

[2] M. Shore and A. D. Fowler, Can. Mineral. **34**, 1111 (1996).

[3] A. Putnis, L. Fernandez-Diaz, and M. Prieto, Nature (London) **358**, 743 (1992); M. Prieto, A. Putnis, and L. Fernandez-Diaz, Geol. Mag. **130**, 289 (1993); M. Prieto, A. Fernandez-Diaz, A. Putnis, and L. Fernandez-Diaz, Geochim. Cosmochim. Acta **61**, 3383 (1997).

[4] P. Ortoleva, *Geochemical Self-Organization* (Oxford University Press, Oxford, 1994).

[5] T. Holten, B. Jamtveit, P. Meakin, M. Cortini, J. Blundy, and H. Austrheim, Am. Mineral. **82**, 596 (1997); T. Holten, B. Jamtveit, and P. Meakin, Geochim. Cosmochim Acta **64**, 1893 (2000).

[6] Y. Wang and E. Merino, Geochim. Cosmochim. Acta **54**, 1627 (1990); **56**, 587 (1992); J. Petrol. **34**, 369 (1993); I. L'Heureux, Phys. Rev. E **48**, 4460 (1993); I. L'Heureux and A. D. Fowler, Geophys. Res. Lett. **23**, 17 (1996).

[7] J.-H. Wang and J.-P. Wu, Eur. J. Mineral. **7**, 1089 (1995).

[8] I. L'Heureux and A. D. Fowler, in *Growth, Dissolution and Pattern Formation in Geosystems*, edited by B. Jamtveit and P. Meakin (Kluwer, Dordrecht, 1999), p. 85.

[9] A. D. Fowler and I. L'Heureux, Can. Mineral. **34**, 1211 (1996).

[10] G. M. Anderson, Econ. Geol. **70**, 937 (1975); D. A. Sverjensky, *ibid.* **76**, 1848 (1981).

[11] G. M. Anderson and R. W. Macqueen, Geosci. Can. **9**, 108 (1982).

[12] G. M. Anderson, Econ. Geol. **86**, 909 (1991).

[13] G. S. Plumlee, D. L. Leach, A. H. Hofstra, G. P. Landis, E. L. Rowan, and J. G. Viets, Econ. Geol. **63**, 451 (1994).

[14] R. E. Liesegang, Photogr. Arch. **21**, 221 (1896); K. H. Stern, Chem. Rev. **54**, 79 (1954); H. K. Henisch, *Periodic Precipitation* (Pergamon, Oxford, 1991).

[15] A. E. Boudreau, S. Afr. J. Geol. **97**, 473 (1994); Mineral Petrol. **54**, 55 (1995).

[16] W. Ostwald, *Lehrbuch der Allgemeinem Chemie* (Engelman, Leipzig, 1897); S. Prager, J. Chem. Phys. **25**, 279 (1956); D.

A. Smith, *ibid.* **81**, 3102 (1984); G. T. Dee, Phys. Rev. Lett. **57**, 275 (1986); M. E. Le Van and J. Ross, J. Phys. Chem. **91**, 6300 (1987).
[17] H. W. Morce and G. W. Pierce, Phys. Chem. **45**, 589 (1903); K. Jablczynski, Bull. Soc. Chim. Fr. **33**, 1592 (1923).
[18] R. Feeney, S. L. Schmidt, P. Strickholm, J. Chadam, and P. Ortoleva, J. Chem. Phys. **78**, 1293 (1983).
[19] R. Sultan and P. Ortoleva, Physica D **63**, 202 (1993).
[20] H. L. Barnes, in *Geochemistry of Hydrothermal Ore Deposits*, 2nd ed., edited by H. L. Barnes (Wiley, New York, 1979), p. 404.
[21] D. Stauffer, J. Aerosol Sci. **7**, 319 (1976).
[22] I. V. Markov, *Crystal Growth for Beginners* (World Scientific, Singapore, 1996).
[23] R. Defay, I. Prigogine, A. Bellemans, and D. H. Everett, *Surface Tension and Adsorption* (Longmans, Green, London, 1966).
[24] F. O. Koenig, J. Chem. Phys. **18**, 449 (1950).
[25] M. Chacron and I. L'Heureux, Phys. Lett. A **263**, 70 (1999).
[26] G. Venzl and J. Ross, J. Chem. Phys. **77**, 1308 (1982).
[27] T. Dewers and P. Ortoleva, Appl. Geochem. **3**, 287 (1988).
[28] D. U. von Rosenberg, *Methods for the Numerical Solution of Partial Differential Equations* (Elsevier, New York, 1969).
[29] W. H. Press, S. A. Teukolsky, W. T. Vetterling, and B. P. Flannery, *Numerical Recipes in FORTRAN*, 2nd ed. (Cambridge University Press, Cambridge, 1992).